ISSN 1027-4510, Journal of Surface Investigation: X-ray, Synchrotron and Neutron Techniques, 2023, Vol. 17, No. 3, pp. 531–541. © Pleiades Publishing, Ltd., 2023.
Russian Text © The Author(s), 2023, published in Poverkhnost', 2023, No. 5, pp. 3–15.

On the Project of Scanning and Projection Microscopes for the Nanoscope Station for Biological Research in the Water Window

I. V. Malyshev[a, *], A. E. Pestov[a], V. N. Polkovnikov[a], D. G. Reunov[a], M. N. Toropov[a], N. I. Chkhalo[a], Ya. V. Rakshun[b], Yu. V. Khomyakov[b], V. A. Chernov[b], and I. A. Shchelokov[c]

[a] *Institute for Physics of Microstructures, Russian Academy of Sciences, Nizhny Novgorod, 603950 Russia*

[b] *Budker Institute of Nuclear Physics, Siberian Branch, Russian Academy of Sciences, Novosibirsk, 630090 Russia*

[c] *Institute for Problems of Microelectronics Technology and High Purity Materials, Russian Academy of Sciences, Chernogolovka, 142432 Russia*

**e-mail: ilya-malyshev@ipmras.ru*

Received July 21, 2022; revised October 17, 2022; accepted October 17, 2022

Abstract—A brief description of the concept of a soft X-ray microscope for the Nanoscope station, which is planned to be installed at the SKIF fourth-generation synchrotron, is given. The microscope is designed to study the structure of cells and dynamic processes in them with nanometer spatial resolution. It will use a unique absorption contrast of ~15 between carbon-containing structures and water in the spectral range of the water window, $\lambda = 2.3–4.3$ nm, which eliminates the need for contrasting and the use of fluorophores and minimizes the doses of ionizing radiation absorbed in the samples to obtain high-quality 3D images. The scanning and projection schemes of the microscope, their main technical characteristics, including the calculated spectra and parameters of the undulator source are presented, and an estimate of the absorbed doses depending on the resolution is obtained. The main advantage of the proposed concept lies in the use of an objective lens of high-aperture multilayer X-ray mirrors, which makes it possible to clearly visualize the focal section of the sample. Technically simple axial tomography will also be used to reconstruct the three-dimensional structure of frozen or dried samples. In the scanning scheme, due to a low dose of radiation, it will be possible to study living plant cells with a resolution of up to 10 nm, animals with a resolution of up to 80 nm, and cryofixed samples with a resolution of up to 5 nm. In the projection scheme, due to simultaneous observation of the entire focal *XY* section, the time for obtaining three-dimensional images is significantly reduced, but due to a large dose, it will be oriented mainly on the study of fixed samples.

Keywords: soft X-ray microscopy, water window, synchrotron radiation, SKIF synchrotron station, study of living cells with nanometer resolution

DOI: 10.1134/S1027451023030114

INTRODUCTION

In modern biological and medical problems to understand the mechanisms of the functioning of biological cells, as well as to study the effect of various diseases on cells [1, 2] it is required to see the component parts of native, ideally living, cells with a resolution of tens of nanometers. To solve this problem, researchers currently have two tools in their arsenal: electron microscopy [3] and optical microscopy with super resolution [4].

The main physical limitation of these methods is the need to use fluorophores in the case of fluorescence methods or contrast in electron microscopy. The use of these substances in itself modifies the object under study. These methods make it possible to observe only structures and molecules bearing a fluorescent label or a contrast agent, while the rest of the sample material, which forms the biological "context" in which the structure under study is located or the process under study proceeds, remains inaccessible for observation.

For more than 30 years, soft X-ray microscopy has been developed in the spectral region of the water window of 2.3–4.3 nm. The uniqueness of this method lies in the following. First, there is a large, ~15, absorption contrast between proteins, fats and carbohydrates, which are based on carbon, in relation to the intercellular fluid (the main absorbing element is oxygen). This eliminates the need for contrast enhancement and minimizes the absorbed dose needed to obtain high-quality images. Secondly, there is practically no scattering, which, together with a sufficiently long radiation path length, makes it possible to study rather thick samples, up to 10 μm or more, which can

even be placed in a cell at normal pressure. More details about the features of the interaction of radiation in this range with biological samples are described in [2].

In view of the relevance of the topic, modern synchrotrons have corresponding stations for soft X-ray microscopy. Microscopes are divided into scanning [5–8] and projection [9–12] types. Both scanning and projection microscopes based on Fresnel zone plates provide high lateral (2D) resolution. For example, in [6], the 2D resolution was less than 10 nm. The situation with volumetric resolution is much worse. In [5], a 3D resolution of 30 nm in the lateral plane and 550 nm along the optical axis was obtained. In the best projection soft X-ray microscopes, in which frozen samples were studied, a volumetric (3D) resolution of 50–60 nm was obtained [9–12]. However, despite the prospects and the demonstration of a number of undoubted achievements, soft X-ray microscopy has not become an important tool in cell biology.

The main reason for this is the shortcomings of the used concept of microscopes based on Fresnel zone plates. The main disadvantages of such plates are low efficiency and angular aperture ($NA < 0.1$). The low efficiency of plates in projection microscopes results in an additional absorbed dose. A low numerical aperture leads to a large (units of micrometers) depth of focus, which severely limits the 3D resolution in a scanning-microscope setup. Projection microscopy for reconstructing the 3D structure of a cell requires the use of a laborious and time-consuming procedure of angular tomography, which, in addition to loss of accuracy, leads to additional absorbed doses.

Therefore, the search for new approaches to the construction of microscopes for the water window is extremely important. The goal of the solutions proposed in this work is to achieve nanometer 3D resolution at the lowest possible absorbed doses in biological samples, ideally, the possibility of observing living cells. To achieve this goal, the Nanoscope station will be developed at the SKIF fourth generation synchrotron, designed to study the structure of cells and dynamic processes in them with nanometer spatial resolution. The paper describes the principles of the microscope construction, its X-ray optical schemes, and the assessment of absorbed doses depending on the resolution.

SELECTION OF MICROSCOPE TYPE, OPTICS AND WAVELENGTH

When choosing the type of microscope, we were guided by the following considerations. Minimal absorbed doses can be achieved using scanning X-ray microscopes. This is due to the fact that in a projection microscope, intensity losses on the X-ray optical elements of the objective lens directly lead to an increase in the absorbed dose. For example, with a scheme efficiency of 10%, in order to achieve the required number of beneficial events, it is necessary to increase the absorbed dose by 10 times. In a scanning microscope, losses on X-ray optical elements lead only to a loss in the intensity of the probe beam and have no effect on the dose absorbed in the sample.

Another advantage of the scanning microscope is that no matrix detectors are required for image acquisition. This makes it possible to increase the recording efficiency to almost 100% and to noticeably (up to MHz) increase the speed of the detector.

However, the use of a scanning microscope for the 3D reconstruction of samples is limited by the depth of focus *DoF* of the focusing optics:

$$DoF \approx \lambda / NA^2, \quad (1)$$

where λ is the working wavelength of the microscope and *NA* is the numerical aperture. It can be seen from relation (1) that in order to achieve a resolution at the wavelength level, high-aperture optics with *NA* approaching unity is required. In the case of Fresnel zone plates $NA < 0.1$ [5–12]; therefore, their longitudinal resolution will be greater than $\pm 100\lambda$. For this reason, this type of optics is not suitable for an ultrahigh resolution scanning microscope.

Multilayer normal-incidence X-ray mirrors deposited onto focusing substrates have large geometric and angular apertures. In particular, on the basis of these elements, lenses for projection lithography at a wavelength of 13.5 nm with a numerical aperture of $NA = 0.3–0.33$ [13, 14] are fabricated and a lens with $NA = 0.55$ is under development [15].

The maximum absorption contrast between proteins and water (about 20), as well as the minimum absorption (absorption length of about 10 μm) can be achieved at a wavelength in the immediate vicinity of the oxygen absorption edge $\lambda_{OK} = 2.33$ nm. For this spectral region, the largest reflection coefficients $R \approx 9\%$ at normal incidence at a wavelength of $\lambda = 2.42$ nm is characteristic of multilayer Cr/V X-ray mirrors [16]. The bandwidth is 0.2%.

Of interest are also Cr/Ti/B_4C and Cr/Sc mirrors. In the first case, at a wavelength of 2.83 nm at normal incidence, the reflectance $R \approx 15.75\%$ was obtained at a spectral bandwidth of 0.3% [17]. However, the results of [16, 17] raise certain doubts, since they are given once and in nonreviewed publications.

Cr/Sc multilayer X-ray mirrors have a record reflectance of $R \approx 23\%$ at a wavelength of 3.12 nm with a spectral bandwidth of 0.3% [18]. For the developed microscope, a pair of Cr/Sc materials was chosen and, accordingly, an operating wavelength of 3.12 nm. This choice was made for the following reasons. First, we have many years of experience in the development and application of Cr/Sc mirrors [19–21]. In [22], the reflection coefficient was obtained for structures without Cr/Sc barrier layers $R \approx 21\%$. We believe that the

Table 1. Basic parameters of the X-ray source

Parameter	Value
Source type × planar vertical undulator:	
Period, cm	5
Number of periods	78
Longitudinal length, m	3.9
Operating wavelength, nm; energy, eV	3.12; 397.4
Beam monochromaticity, %; width level at half maximum (FWHM), eV	2; 8
Size at half maximum intensity (largest), μm	30
Angular divergence, μrad	25
Average intensity of the radiation of the first harmonic in the band 0.1%, 10^{15} photon/s	5.6
Total radiation power, W	500

use of barrier coatings and the nitridation of layers, as in [18], will make it possible to noticeably increase the reflection coefficient. Second, Cr/Sc multilayer X-ray mirrors have both a high reflection coefficient and a wide spectral band, which will increase the intensity of the probe beam and, accordingly, reduce the time of the experiment. Thirdly, in the manufacture of multilayer mirrors for lenses, very stringent requirements are imposed on substrates. To ensure the diffraction quality of the image, according to the Marechal criterion, the root-mean-square aberration of the lens should not exceed $RMS \le \lambda/14$. In the case of $\lambda = 3.12$ nm, this corresponds to the value $RMS \le 0.22$ nm. The fabrication of such substrates is at the limit of modern technologies [23]. Fourth, despite moving away from the oxygen absorption edge, the absorption contrast and absorption length did not decrease much, to 15 and 6 μm, respectively.

As noted above, the advantage of a scanning microscope is the lowest possible dose absorbed in the test sample. However, this scheme of a soft X-ray microscope has one significant drawback. Due to the limited speed of a 3D piezoelectric nanoscanner (for example, [24]), the time of taking a tomogram can reach an hour or more. The scheme of a projection microscope is devoid of this shortcoming, in which the entire *XY* field is recorded at once in one frame, and to restore the 3D structure, the sample moves along the optical axis *Z*. This approach makes it possible to reduce the tomography time to fractions of minutes, and when observing thin samples or selected sections, to fractions of a second. Therefore, to implement both modes of operation, two soft X-ray microscopes (scanning and projection types) will be installed at the Nanoscope station.

X-RAY OPTICAL SCHEME OF A SCANNING MICROSCOPE

When developing the X-ray optical scheme of the microscope, it is necessary to take into account the features of the fourth-generation synchrotron source. The parameters of the X-ray source are given in Table 1. Figures 1 and 2 show the intensities of various harmonics of the source, from which follows: first, a part of the energy of the synchrotron-radiation beam corresponds to high harmonics and must be "removed" so it is not incident on the precision X-ray optical elements of the microscope; secondly, at a distance of 20 m from the source, the size of the X-ray beam at half height of the intensity will be 1 mm (Fig. 3). This is a major problem for the application of mirror optics, since the use of imaging micro-optics is actually required. Taking into account the fact that multilayer X-ray mirrors are Bragg reflectors, the Bragg condition must be satisfied at each point of radiation incidence on the mirror. Obviously, large film-thickness gradients over a total length on the order of 1 mm cannot be obtained.

Another problem is the orientation of the optical axis of the microscope. The axes of the microscopes

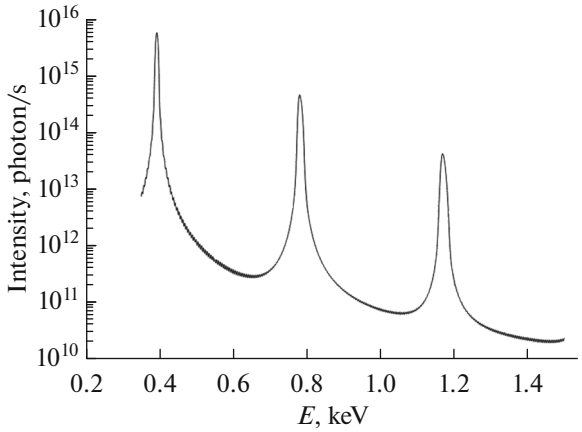

Fig. 1. Intensity of various source harmonics in the 0.1% energy band (ring undulator, $B = 0.39$ T, $\lambda_u = 50$ mm, photon-flux diameter 1 mm at a distance of 20 m from the source, $L_u = 3.9$ m, $N_p = 78$).

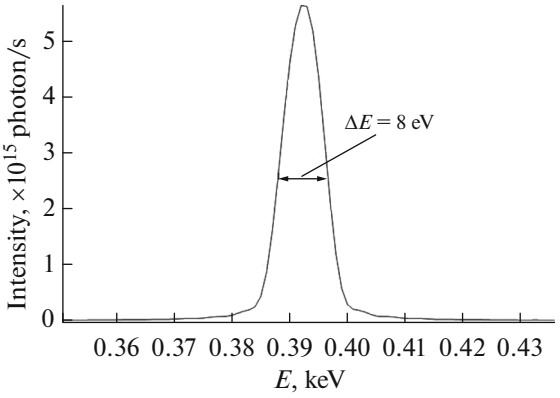

Fig. 2. Intensity of the first harmonic in the 0.1% energy band.

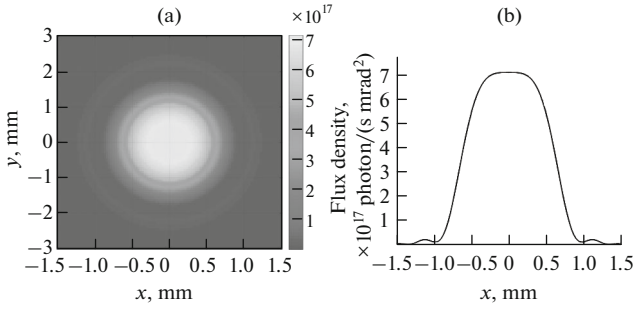

Fig. 3. Calculated beam at a distance of 20 m from the synchrotron-radiation source; cross section in the 0.1% energy band: (a) *XY*; (b) *X*.

described in the works mentioned above are located horizontally, in the plane of the synchrotron orbit. From the point of view of ergonomics and convenience of working with samples, this is an inconvenient orientation. Usually all microscopes have a vertical optical axis.

In the present project, both of these problems are solved by the hybrid scheme of the microscope, which includes reflective and diffractive X-ray optical elements. The X-ray optical scheme of a scanning soft X-ray microscope is shown in Fig. 4, the main elements and their relative position are described in Table 2. Radiation from the undulator, propagating along the channel, is incident on a system of two flat mirrors *1* (Fig. 4). The system of mirrors performs the functions of a high harmonic filter and an attenuator of the intensity of the X-ray beam entering the microscope. For example, Fig. 5 shows the spectral dependence of the reflection coefficient from a silicon mirror at an angle of radiation incidence of 3°. As can be seen from the figure, with a reflection coefficient of the first (working) harmonic of 55%, suppression of the second harmonic will be about 16 times, respectively, with a double reflection of about 260. The position relative to the source and the parameters of the mirrors (angle of incidence, coating material) will be further optimized to ensure closeness to 100% reflection. Nevertheless, it can be seen that such a system ensures the almost complete suppression of all harmonics, which does not require further cooling of the microscope mirrors. The absence of strong thermal loads is of fundamental importance to prevent distortion of the wavefronts.

Proceeding further, the radiation is incident on the first element of the nanoscope, i.e., the Bragg—Fresnel lens *5* (Fig. 4) [25]. A Cr/Sc coating will be used as the reflective one. The Bragg–Fresnel lens performs several functions at once. Firstly, it performs the first stage of X-ray focusing to a size of about 0.125 μm (200 times reduction). Secondly, it rotates the beam by 90°, thereby providing a convenient orientation of the optical axis of the microscope. Third, since a quasi-monochromatic beam is incident on the lens, its fabrication does not require the deposition of a multilayer mirror with a period gradient over the surface.

A diaphragm with a submicron aperture is set in the focusing plane. The aperture acts as a filter for cutting off the tails of the probe beam. The diverging beam is incident on a Schwarzschild lens. The numerical aperture lens $NA = 0.4$ further reduces the size of the focus in the sample plane by a factor of 54. The calculated intensity distribution of the probe beam, limited by diffraction, is shown in Fig. 6. The transverse size of the image is FWHM = 5 nm. Thus, potentially the X-ray optical scheme provides a lateral resolution at the level of 5 nm.

The test sample is placed in the image plane. The radiation transmitted through the sample is recorded by a detector (pin diode, microchannel plate) synchronized with the electron bunches of the synchrotron. To reconstruct the 3D structure, the sample is placed on a scanner table that moves the sample along three coordinates *x*, *y* and *z* with nanometer precision. A table from PI, model P-561.3DD, was chosen as the scanner. The technical characteristics of the scanner, taken from [24], are given in Table 3.

The measurement technique and reconstruction of the 3D structure are similar to confocal microscopy, except for the absence of fluorophores and the fact that a useful signal is formed over the entire volume of the sample, while in confocal microscopy only areas with a fluorophore give a signal. The samples for research can be either fixed via freezing in liquid nitrogen vapor or placed in special cuvettes under normal conditions.

To reduce wavefront deformations and ensure the dimensional stability of the X-ray optical scheme under conditions of high-power X-ray fluxes, the first mirror of the two-mirror system will be cooled with liquid nitrogen or water, which will be determined in more detail, and the second mirror will be cooled with water. Subsequent elements, due to the rather low

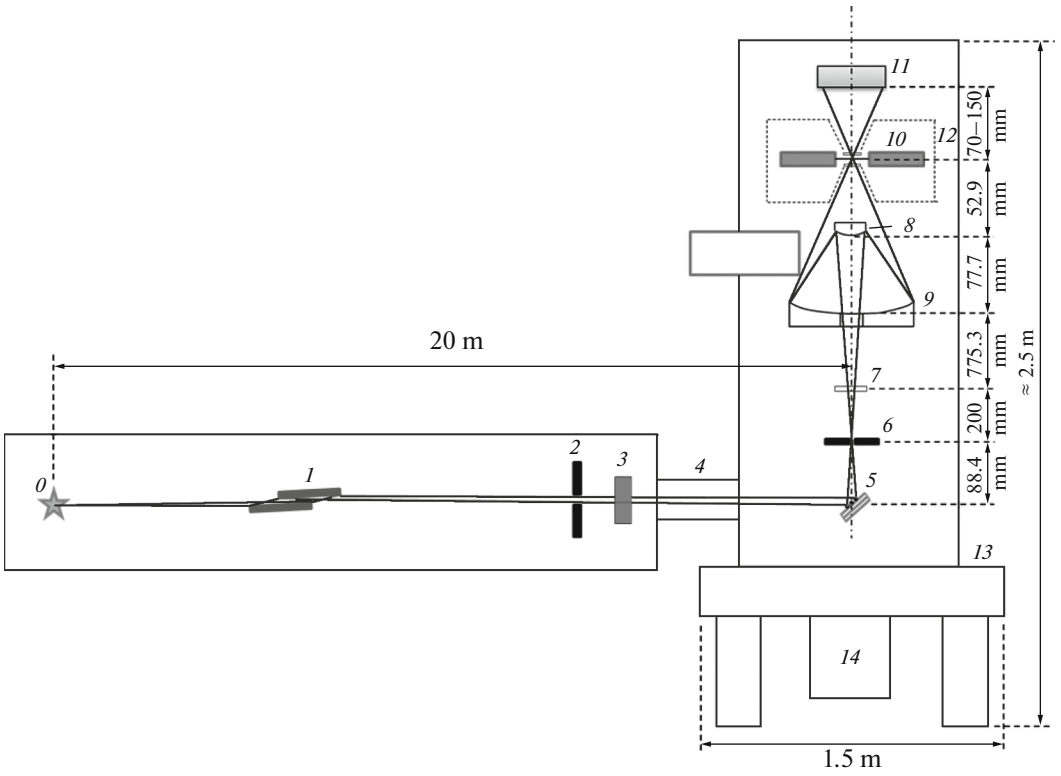

Fig. 4. X-ray optical scheme of the scanning microscope at the Nanoscope station: *1* is two flat mirrors; *2* is the output aperture of the front end; *3* is the X-ray beam visualizer; *4* is bellows with gates; *5* is the Bragg–Fresnel lens; *6* is the diaphragm; *7* is the set of filters; *8* is the primary mirror *M*1 of the lens 54×; *9* is the secondary mirror *M*2 of the lens 54×; *10* is the sample; *11* is the detector; *12* is the cryochamber; *13* is the vibration isolation system; *14* is the vacuum system.

power of radiation cleared of harmonics, do not require forced cooling, and passive (radiator) cooling will be sufficient.

In order to maintain the dimensional stability of the X-ray optical scheme, materials with low, at a level of 10^{-8}–10^{-7} K^{-1}, temperature coefficients of linear expansion (ULE, astrositall and titanium-niobium alloy TV-36). In addition, the lens housing will be thermally stabilized.

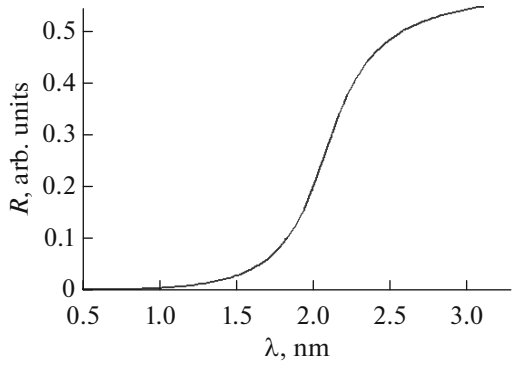

Fig. 5. Harmonic filter. Spectral dependence of the reflection coefficient of a silicon mirror at a grazing incidence angle of 3°. The suppression of the second harmonic with double reflection reaches 260.

ESTIMATION OF THE PROBE-BEAM INTENSITY IN A SCANNING SOFT X-RAY MICROSCOPE

Estimation of the probe-beam intensity *PBI* can be determined from the following relation:

$$PBI = I_{SR}\Delta\lambda_M R_{BFL} R_{GIM}^2 R_{MLM}^2 \ [\text{photon/s}], \quad (2)$$

where I_{SR} is the intensity of radiation from the undulator, expressed in photons emitted per second in the spectral band of 0.1%; $\Delta\lambda_M$ is the spectral transmission bandwidth of the optical system, expressed in fractions of the 0.1% bandwidth; R_{BFL} is the efficiency of the Bragg–Fresnel lenses; R_{GIM} is the reflection coefficient of the grazing incidence mirror; and R_{MLM} is the reflection coefficient of the Cr/Sc multilayer mirror. Substituting into relation (2) the expected values $I_{SR} = 5.6 \times 10^{15}$ photon/s (Table 1), $\Delta\lambda_M = 2.4$ (microscope bandpass 0.24%), $R_{BFL} = 0.3$, $R_{GIM} = 0.8$ (value after mirror-coating optimization) and $R_{MLM} = 0.2$ (the current level of manufacture of the Cr/Sc mirror), we obtain $PBI = 1 \times 10^{14}$ photon/s.

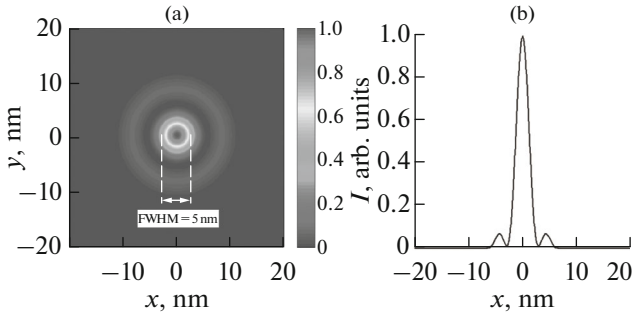

Fig. 6. Image (a) and cross section of the focus (b) of an Xpray probe beam in the scheme of a scanning soft X-ray microscope.

ESTIMATION OF THE ABSORBED DOSE DEPENDING ON THE SPATIAL RESOLUTION

To obtain high-quality X-ray images, it is necessary that the number of recorded events be at least 25. In this case, the Poisson noise will be 20%. Since the image contrast between water and proteins exceeds 10, for estimation it can be assumed that all absorption events occur in the protein. In this case, to ensure a resolution with a lateral dimension d in a cube with the volume d^3 25 photons must be absorbed. Accordingly, in the scheme of a scanning soft X-ray microscope, the absorbed dose D in Gray can be expressed as:

$$D(d) = 1.6 \times 10^{-19}\, NE_{\text{ph}} \big/ (d^3 \rho), \qquad (3)$$

where N is the number of photons needed to restore the image, E_{ph} is the photon energy in eV, the multiplier is the conversion of energy from electron volts to joules, and ρ is the density. Substituting the expected values ($N = 25$, $E_{\text{ph}} = 397$ eV, $\rho = 10^3$ kg/m^3), expression (3) can be rewritten in a form showing the dependence of the dose on the resolution d:

$$D(d) = 1.6 \times 10^8 \big/ d^3 \left[\text{Gray} \big/ \text{nm}^3\right]. \qquad (4)$$

Figure 7 shows the dependence of the required dose on the resolution, calculated according to (4). From the above dependence, the following can be distinguished. First, even with a resolution of 1 nm, the required dose does not exceed the allowable 10^8 Gray [26] to preserve frozen cells in their native state; there-

Table 2. Optical elements of the Nanoscope station

No.	Element	Distance from previous element	Description
0	SR source	0	Undulator
1	Two flat mirrors	15 m	Cooled harmonic filter – beam intensity attenuator
2	Front-end output aperture	13 m	System of cooled slots that emit a central radiation cone with $NA = 25$ mrad
3	X-ray beam visualizer	0.5 m	Beam position and intensity monitors
4	Bellows with gates	0.5 m	
5	Bragg–Fresnel lens	1 m	Multilayer Cr/Sc mirror with an elliptical zone plate on the surface, tilted by 45°. The working region is an ellipse ($2a = 1.4$ mm, $2b = 1$ mm), cooled by LN_2
6	Diaphragm	88.4 mm	1-μm diaphragm cooled by H_2O
7	Filter set	200 mm	Multilayer filters for incident-radiation-flux control
8	Primary mirror $M1$	853 mm	Convex mirror Cr/Sc of the Schwarzschild objective, which creates a 1-μm aperture image on the sample with a reduction of 54 times $R = -28.2$ mm, $D = 12$ mm $NA = 0.4$
9	Secondary mirror $M2$	77.7 mm	Concave mirror Cr/Sc of the Schwarzschild objective. $R = -107.6$ mm, $D = 78$ mm
10	Sample	130.6 mm	Sample on the X, Y, Z scanner with feedback (Table 3)
11	Detector	70–150 mm	Pin diode or microchannel plate that records the signal passing through the observed points of the sample
12	Cryochamber		It is possible to install a cryochamber with sample cooling by LN_2 vapors
13	Vibration isolation system		Optical table; spring suspension of the optical farm; magnetic damper on Foucault currents
14	Vacuum system		High vacuum pumping

Table 3. Characteristics of the *X*, *Y*, *Z* sample table of PI (model P-561.3DD) (taken from [24])

Characteristic	P-561.3DD
Movement direction	*X*, *Y*, *Z*
Displacement speed, mm/s	0.2
Built-in sensor	Capacitive
Movement range without feedback (from –20 to +120 V), μm	58 × 58 × 18
Movement range with feedback, μm	45 × 45 × 15
Resolution without feedback, nm	0.1
Resolution with feedback, nm	0.2
Nonlinearity, %	0.01
Repeat positioning accuracy *X*, *Y*, *Z*, nm	2
Pitch when moving along the axes *X*, *Y*, μrad	±3
Runout of *X*, *Y* when moving along the axis *Z*, μrad	±3
Yaw when moving along the axes *X*, *Y*, μrad	±3
Plane parallelism in the plane *X*, *Y*, nm	±10
Crosstalk along the axes *X*, *Y* when moving along the axis *Z*, nm	±20
Operating temperature range, °C	–20 to +80
Material	Aluminum
Weight, kg	1.55
Cable length, m	1.5
Recommended controller	E-725, E-712

fore, the resolution is no longer limited by the dose, but by the probe-beam size of 5 nm. Secondly, the maximum allowable dose of 300 Gray, at which the vital activity of animal cells is preserved [2], corresponds to the maximum resolution of 80 nm. Thirdly, the maximum allowable dose of 10^4–10^5 Gray, at which the vital activity of plant cells is preserved [27, 28], corresponds to the limiting resolution of 10–25 nm.

ESTIMATION OF THE EXPOSURE TIME FOR THE RECOVERY OF A 3D STRUCTURE IN A SCANNING SOFT X-RAY MICROSCOPE

Without taking into account the time losses spent moving the scanner, the time required to obtain 3D tomographic data T_{exp} is determined by the sample size $L \times W \times H$, resolution d, intensity of the probe beam on the sample PBI and the number of photons N_{ph} absorbed in a cube with a side equal to the resolution. The relationship between these parameters can be expressed as:

$$T_{exp} = (N_{ph} LWH)/(PBId^3)\ [\text{c}]. \quad (5)$$

For a sample of cubic form, expression (5) can be rewritten as:

$$T_{exp} = (N_{ph} L^3)/(PBId^3)\ [\text{c}]. \quad (6)$$

Substituting into (6) the values $N_{ph} = 25$ photons and $PBI = 1 \times 10^{14}$ photon/s, we get

$$T_{exp} = 2.4 \times 10^{-13}\, L^3/d^3\ [\text{c}]. \quad (7)$$

For example, for a cell of size 10 × 10 × 10 μm and 20 nm resolution, it will take 3×10^{-5} s. Thus, the main limitation is not the power of the X-ray source, but the speed of the scanner. For the considered case, the full scan time will be about 3.5 hours. Since the scan time is inversely proportional to the cube of the spatial res-

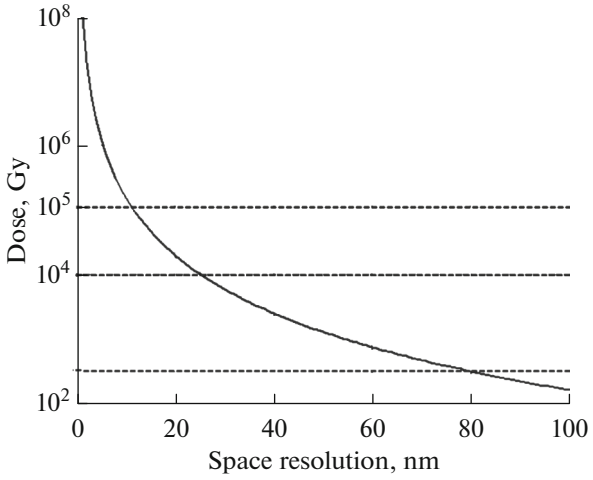

Fig. 7. Dose dependence on the spatial resolution in a scanning soft X-ray microscope. Solid horizontal lines mark the level of doses below which nonfrozen cells retain their vital activity (upper for plants, lower for animals).

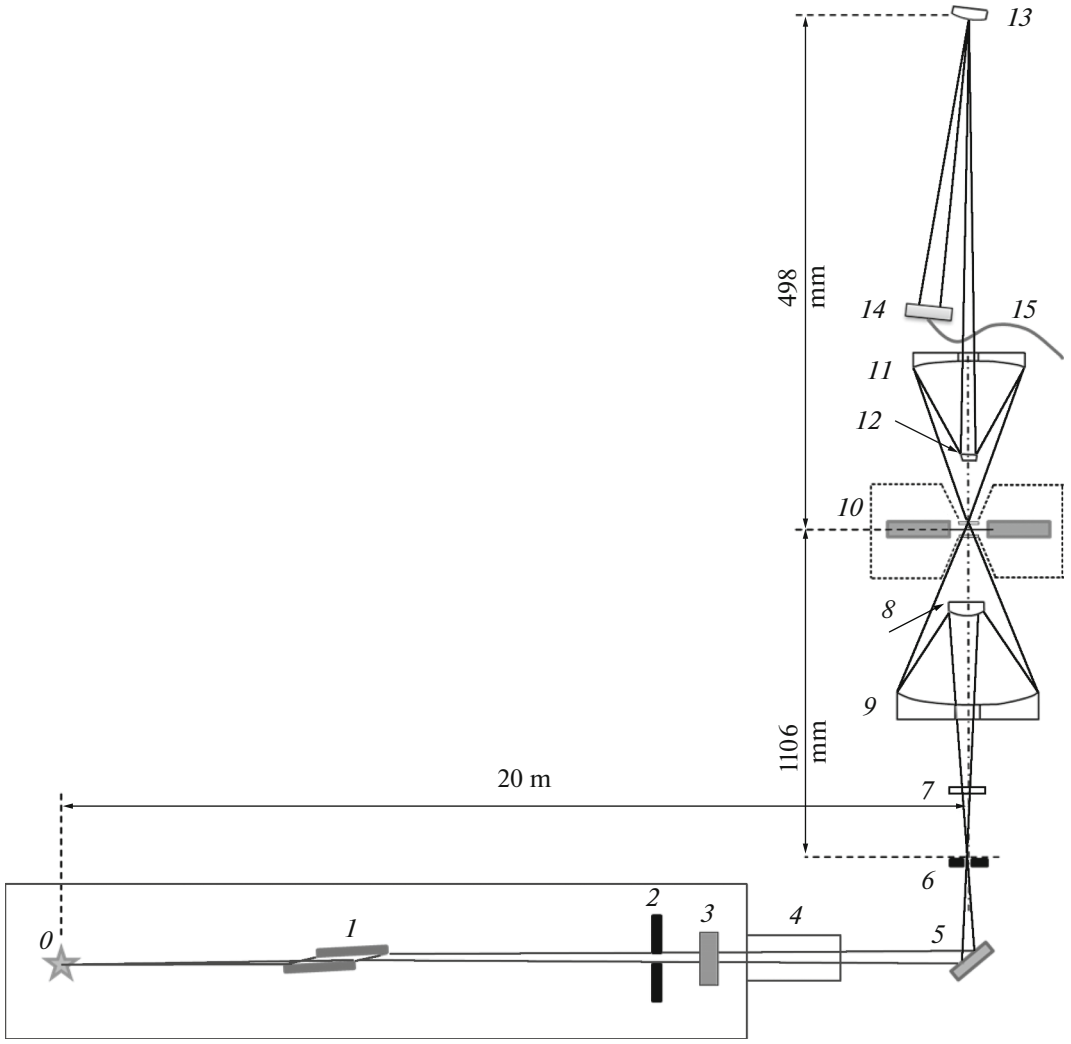

Fig. 8. X-ray optical projection scheme of the channel and station. Designations as in Fig. 4.

olution (i.e., the cube of the scan step), when studying dynamic processes, where the expected resolution is 80 nm, the measurement time for a cell of size 10 × 10 × 10 μm will be reduced to about 3 min, and its focal section to 15 ms!

FULL FIELD PROJECTION MICROSCOPE

The first half of the projection scheme (elements *0*–*7* in Fig. 8) exactly repeats the scanning scheme (Fig. 4). Next comes a two-mirror lens illuminator, consisting of mirrors *8* and *9*. In contrast to the objective lens of the scanning scheme, it must collect radiation not at a point, but illuminate a field of view 16.6 × 16.6 μm in size (equal to the size of the detector matrix 13.3 × 13.3 mm divided by a magnification of 800×) on the sample *10*; therefore, the requirement for the accuracy of the shape of the optics is moderate. A magnified sample image is projected by a three-mirror objective lens *11*–*13* (Fig. 8) onto the matrix camera *14*. A magnification of 800x is optimal so that, on the one hand, the pixel size in the subject area is small and equal to 8 × 8 nm, and, on the other hand, the field of view is sufficient to observe most cells. A description of the main elements of the projection scheme and their relative position is given in Table 4.

The projection lens was about 500 mm high and 100 mm wide, compact enough for such a large magnification. The small convex mirror diameter of 12.6 mm is large enough for the mechanical and ion polishing of rough surfaces and a reflective multilayer coating. The calculated lens aberrations for all field points are subnanometer. This provides an energy fraction, close to the diffraction limit (Fig. 9a, upper curve), of the focusing spot in one pixel with a size of 6.5 μm from 51 to 62%, depending on the field point. Figure 9b shows how the focus spot on the recording matrix fits into pixels.

Recording and processing the sample images will be carried out as follows. The sample will be shifted

Table 4. Optical elements of the projection microscope for the Nanoscope station

No.	Element	Distance from the previous element, mm	Description
0	SR source	0	Undulator
1	Two flat mirrors	15000	Cooled harmonic filter – beam intensity attenuator
2	Front-end output aperture	3000	A system of cooled slots that emit a central radiation cone with $NA = 25$ mrad
3	X-ray beam visualizer	500	Beam position and intensity monitors
4	Bellows with gates	500	
5	Bragg–Fresnel lens	1000	Multilayer Cr/Sc mirror with elliptical zone plate on the surface, inclined by 45°. The working region is an ellipse ($2a = 1.4$ mm, $2b = 1$ mm), cooled H_2O or LN_2
6	Diaphragm	88	Diaphragm cooled by H_2O
7	Filter set	200	Multilayer filters for incident-radiation-flux control
8	Primary mirror of the Schwarzschild condenser objective	853	Convex Cr/Sc mirror of the Schwarzschild condenser objective, which increases the beam aperture by a factor of 50 to 0.28 and creates a uniform illumination field on the sample. $R = -28.2$ mm, $D = 12$ mm
9	Secondary mirror of the Schwarzschild condenser objective	77	Concave mirror Cr/Sc condenser lens $R = -107.6$ mm, $D = 78$ mm
10	Sample	130	Sample on a Z scanner with feedback
11	Primary lens mirror ×800	166.3	Concave mirror projection lens $R = 133.3$ mm, $D = 100$ mm, $D_{light} = 92$ mm
12	Secondary lens mirror ×800	95.9	Convex mirror projection lens $R = -31.1$ mm, $D = 12.6$ mm
13	Tertiary lens mirror ×800	401.4	Convex mirror projection lens $R = -16.3$ mm, $D = 20$ mm, $D_{light} = 0.6$ mm
14	Recording matrix	265, angle 4° to the horizontal	GPIXEL GSENSE2020BSI Pulsar with a field size 2048 × 2048 pixels and 6.5 μm pixel size
15	Matrix cooling		Copper cold pipe, from the “cold finger”, cooled by liquid-nitrogen vapor from the outside of the vacuum chamber

along the optical axis, and a series of images of its sections will be obtained $I(x', y')$, where x', y' are coordinates on the recording matrix. Further, in standard programs, for example, in ImageJ with the DeconvolutionLab2 plugin [29], the following equation is iteratively solved:

$$\mu = -\ln\left(I/I_0\right)\Big/\Delta L \otimes^{-1} h, \qquad (8)$$

where I_0 is the intensity of the sample illumination field when there is no sample, h is the point spread function, taking into account diffraction, aberrations and conical convergence of the rays to the imaged point and conical exit from it, $\mu(x, y, z)$ is the desired three-dimensional absorption coefficient of cell structures, and $\otimes^{-1}$ is the deconvolution operator. To improve the quality of the image, before deconvolution, noise will be eliminated, the average intensity will be normalized in XY cuts and eliminate XY displacement in the case of the Z scan. This approach proved to be excellent in the reconstruction of three-dimensional images in a laboratory microscope of extreme ultraviolet (EUV) radiation with absorption contrast that was put into operation [29].

ESTIMATION OF THE EXPOSURE TIME FOR RECOVERY OF THE 3D STRUCTURE IN THE PROJECTION SCHEME

The tomography time is the sum of the time for z movement of the stage and exposure time of all frames T_{exp}. The time of z movement of the stage by 30 μm is 0.15 s, since the speed of movement of the PI stage is

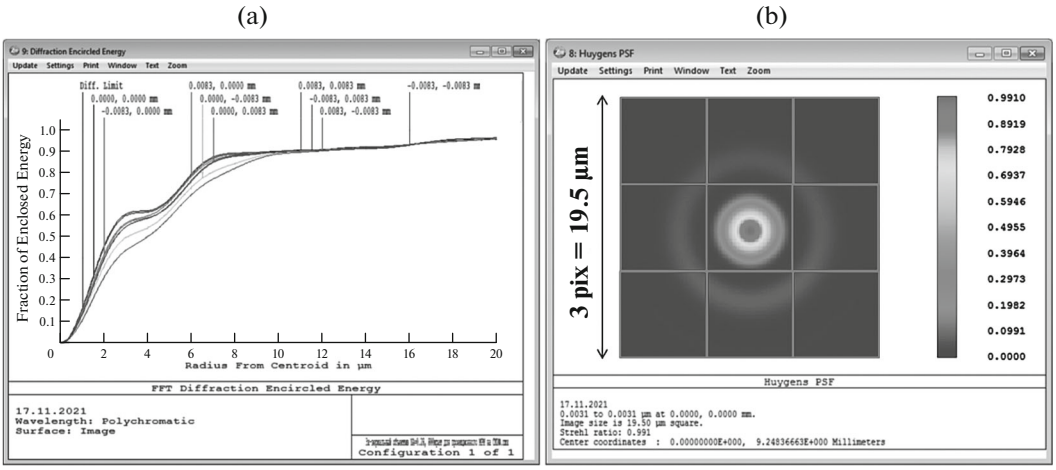

Fig. 9. Energy distribution in the focus spot for different field points (center and edges of the matrix (a)). Focus spot in the center of the field of view on a GPIXEL 2020BSI Pulsar CMOS sensor (b).

0.2 mm/s [24]. The exposure time for all frames T_{exp} is determined by the formula:

$$T_{\text{exp}} = \frac{C_{\text{pix}} E_e N_{\text{pix}}}{E_p PBI} \frac{H}{\Delta h} k, \tag{9}$$

where $C_{\text{pix}} = 55 \times 10^3 \overline{e}$ is the pixel capacity, $E_e = 3.6$ eV is the energy spent on the creation of one electron–hole pair in a semiconductor pixel, $E_p =$ 397 eV is the energy of a photon with a wavelength of 3.12 nm, $PBI = 1 \times 10^{12}$ s^{-1} is the intensity of the beam illuminating the sample, taking into account the reflection from five mirrors [30], $\frac{H}{\Delta z}$ is the number of steps along the axis z, $H = 20$ μm is the movement of the stage along the axis z for recording a sample with a thickness of 10 μm and its surroundings, $\Delta z = 16$ nm is the z step, and k is the intensity attenuation coefficient due to absorption in the sample. For example, when radiation with a wavelength of 3.12 nm passes through a sample (cell 10 × 10 × 10 μm in a layer of ice 20 μm thick) coefficient

$$\begin{aligned} k &= \exp(-(\mu_{\text{ice}} H_{\text{ice}} + \mu_{\text{protein}} H_{\text{protein}})) \\ &\approx \exp\left(-\left(1/4\right)20\right) \approx 150. \end{aligned} \tag{10}$$

Substituting these numbers into (9), we get that $T_{\text{exp}} =$ 10 min. Since this time is calculated from the condition that the entire pixel capacity is filled, the noise must be small, and this is very important for the deconvolutional reconstruction of a 3D image.

Let us estimate the time to save frames in the computer memory for a thickness of 20 μm with a z step of 16 nm. It will be 10 minutes at a storage rate of 2 fps. Since this time is equal to the exposure time of all frames, signal accumulation and storage of the frame obtained at the previous $z$step, can be implemented simultaneously, so the tomography time will not increase and will be the same, i.e., 10 minutes.

Thus, the scanning scheme is better suited for studying live samples, because it provides dose lower by three orders of magnitude, and the projection scheme is better suited for studying chemically fixed or frozen samples, because the acquisition time is about 300 times faster.

CONCLUSIONS

The concept and X-ray optical scheme of the Nanoscope station, which is planned to be installed at the SKIF fourth-generation synchrotron, are described. The station is designed to study the structure of cells and dynamic processes in them with nanometer spatial resolution in the spectral region of the water window. The novelty of the approach is the use of multilayer X-ray mirrors for the formation of a probe beam. Due to the large numerical aperture of the Schwarzschild objective compared to the Fresnel zone plate, the depth of focus (area of sharp focusing) of the probe beam is $DoF = \lambda/NA^2 = 20$ nm for $\lambda =$ 3.12 nm and $NA = 0.4$, which makes it possible to use Z tomography instead of angular tomography which is more complex, less accurate and increases the dose absorbed in the sample. Also, the shallow depth of focus makes it possible to study the dynamics of living cells with nanometer resolution by tracking a sharply imaged focal section in the scanning scheme (with a millisecond time resolution) or by a complete XYZ scan (with a time resolution of one minute).

When constructing schemes of an X-ray microscope, a hybrid scheme of beam transportation to the sample was proposed for the first time, including Bragg–Fresnel optics and mirror optics, which makes it possible to work with small X-ray beams.

The calculations show that in the entire range of resolutions provided by soft X-ray microscopy, due to the unique absorption contrast between proteins and water, even living samples can be studied with a resolution of up to 10 nm (for plant cells), and frozen samples with a resolution of up to 5 nm in a scanning scheme and up to 8 nm in the projection scheme.

We expect that work at the station will make it possible to find new niches for microscopy in the water window and will also allow advances in resolution and speed of research compared to similar microscopes installed on synchrotrons.

FUNDING

This work was supported by the Russian Science Foundation (grant no. 22-62-00068).

CONFLICT OF INTEREST

The authors declare that they have no conflicts of interest.

REFERENCES

1. E. Hanssen, C. Knoechel, M. Dearnley, et al., J. Struct. Biol. **177**, 224 (2012). https://doi.org/10.1016/j.jsb.2011.09.003
2. J. Kirz, Q. Rev. Biophys. **28**, 33 (1995). https://doi.org/10.1017/s0033583500003139
3. M. Eltsov, D. Grewe, N. Lemercier, et al., Nucleic Acids Res. **46**, 9189 (2018). https://doi.org/10.1093/nar/gky670
4. S. W. Hell and J. Wichmann, Opt. Lett. **19**, 780 (1994). https://doi.org/10.1364/OL.19.000780
5. A. Späth, S. Schöll, C. Riess, et al., Ultramicroscopy **144**, 19 (2014). https://doi.org/10.1016/j.ultramic.2014.04.004
6. J. Vila-Comamala, K. Jefimovs, J. Raabe, et al., Ultramicroscopy **109**, 1360 (2009). https://doi.org/10.1016/j.ultramic.2009.07.005
7. A. Spath, J. Raabe, and R. H. Fink, J. Synchrotron Radiat. **22**, 113 (2015). https://doi.org/10.1107/S1600577514022322
8. Y. Kotani, Y. Senba, K. Toyoki, et al., J. Synchrotron Radiat. **25**, 1444 (2018). https://doi.org/10.1107/S1600577518009177
9. P. A. C. Takman, H. Stollberg, G. A. Johansson, et al., J. Microsc. **226**, 175 (2007). https://doi.org/10.1111/j.1365-2818.2007.01765.x
10. C. A. Larabell and M. A. Le Gros, Mol. Biol. Cell **15**, 957 (2004). https://doi.org/10.1091/mbc.E03-07-0522
11. I. V. Malyshev, A. E. Pestov, V. N. Polkovnikov, et al., J. Surf. Invest.: X-ray, Synchrotron Neutron Tech. **12**, 1253 (2018). https://doi.org/10.1134/S1027451019010129
12. G. Schneider, P. Guttmann, S. Heim, et al., Nat. Methods **7**, 985 (2010). https://doi.org/10.1038/nmeth.1533
13. N. I. Chkhalo, I. V. Malyshev, A. E. Pestov, et al., Appl. Opt. **55**, 619 (2016). https://doi.org/10.1364/AO.55.000619
14. B. Turkot, Proc. SPIE **9776**, 977602 (2016). https://doi.org/10.1117/12.2225014
15. A. Pirati, J. V. Schoot, K. Troost, et al., Proc. SPIE **10143**, 101430 (2017). https://doi.org/10.1117/12.2261079
16. E. M. Gullikson, F. Salmassi, A. L. Aquila, and F. Dollar, Progress in short period multilayer coatings for water window applications (Lawrence Berkeley Natl. Lab., Berkeley, 2006). http://escholarship.org/uc/item/8hv7q0hj. Accessed June 20, 2008.
17. Z. Jingtao, L. Haochuan, W. Hongchang, et al., PXRNM Workshop-2016 (2016). https://www.utwente.nl/en/tnw/xuv/workshops/archive/pxrnm-workshop-2016/program/pxrnms-2016-abstracts-poster-presentations.pdf.
18. C. Burcklen, S. de Rossi, E. Meltchakov, et al., Opt. Lett. **42**, 1927 (2017). https://doi.org/10.1364/OL.42.001927
19. S. S. Andreev, M. S. Bibishkin, N. I. Chkhalo, et al., J. Synchrotron Radiat. **10**, 358 (2003). https://doi.org/10.1107/S0909049503015255
20. M. S. Bibishkin, N. I. Chkhalo, A. A. Fraerman, et al., Nucl. Instrum. Methods Phys. Res., Sect. A **543**, 333 (2005). https://doi.org/10.1016/j.nima.2005.01.251
21. A. D. Akhsakhalyan, E. B. Kluenkov, A. Ya. Lopatin, et al., J. Surf. Invest.: X-ray, Synchrotron Neutron Tech. **11**, 1 (2017). https://doi.org/10.1134/S1027451017010049
22. V. N. Polkovnikov, S. A. Garakhin, D. C. Kvashennikov, I. V. Malyshev, N. N. Salashchenko, M. V. Svechnikov, R. M. Smertin, and N. I. Chkhalo, Tech. Phys. **65**, 1809 (2020).
23. N. I. Chkhalo, I. V. Malyshev, A. E. Pestov, et al., Phys.—Usp. **63**, 67 (2020). https://doi.org/10.3367/UFNe.2019.05.038601
24. http://www.eurotek-general.ru/products/systems_pi/multicoordinate/p-561-p-562-p-563-pimars/"\l"ad-image-0.
25. I. A. Schelokov, D. V. Roshchupkin, A. S. Kondakov, et al., Opt. Commun. **159**, 278 (1999). https://doi.org/10.1016/S0030-4018(98)00598-7
26. G. Schneider and B. Niemann, X-Ray Sci. **2**, 8 (1994).
27. J. R. Gilbert, Soft X-ray microimaging of whole wet Cells, PhD Thesis (California Inst. Technol., Pasadena, CA, 1992).
28. N. I. Chkhalo, I. V. Malyshev, A. E. Pestov, V. N. Polkovnikov, D. G. Reunov, N. N. Salashchenko, I. A. Shchelokov, AIP Conf. Proc. **2299**, 060005 (2020). https://doi.org/10.1063/5.0031702
29. I. V. Malyshev, D. G. Reunov, N. I. Chkhalo, et al., Optics Express 30(26), 47567 (2022). https://doi.org/10.1364/OE.475032
30. D. Sage, L. Donati, F. Soulez, et al., Methods **115**, 28 (2017). https://doi.org/10.1016/j.ymeth.2016.12.015